Materials Science & Engineering C 110 (2020) 110728

Contents lists available at ScienceDirect

Materials Science & Engineering C

journal homepage: www.elsevier.com/locate/msec

Strengthening mechanism and corrosion resistance of beta-type Ti-Nb-Zr-Mn alloys

S.F. Jawed[a], C.D. Rabadia[a], Y.J. Liu[b], L.Q. Wang[c,*], P. Qin[a], Y.H. Li[d], X.H. Zhang[d], L.C. Zhang[a,*]

[a] School of Engineering, Edith Cowan University, 270 Joondalup Drive, Joondalup, Perth, WA 6027, Australia
[b] School of Engineering, The University of Western Australia, 35 Stirling Highway, Perth, WA 6009, Australia
[c] State Key Laboratory of Metal Matrix Composites, School of Material Science and Engineering, Shanghai Jiao Tong University, No. 800 Dongchuan Road, Shanghai 200240, China
[d] School of Mechanical Engineering, Xi'an University of Science and Technology, Xi'an 710054, China

ARTICLE INFO

Keywords:
Titanium alloy
Microstructure
Strengthening mechanism
Strain hardening index
Corrosion resistance

ABSTRACT

In order to achieve an effective balance between plasticity and strength, a group of Ti-26Nb-xZr-yMn (x = 4, 7, 10 wt% and y = 3, 5 wt%) alloys were designed to evaluate the effects of Mn and Zr on the microstructures, mechanical properties and strengthening effects of the Ti—Nb system. All the investigated alloys illustrate a monolithic β phase in their microstructure and they all possess substantial true plasticity (~160%) and true maximum strength (~ 950 MPa) without fracture during the compression tests within the load capacity of 100 kN. The contribution of solid-solution, grain-boundary and dislocation strengthening mechanisms have been evaluated using the strengthening model for β Ti alloys for all the investigated alloys. Among the investigated alloys, Ti-26Nb-4Zr-5Mn demonstrates the highest true yield strength (654 MPa), dislocation density (2.45×10^{15} m^{-2}) and hardness (242 HV) along with improved strain hardening ability in terms of strain hardening indices (0.42 and 0.09). Furthermore, based on the superior mechanical properties among the investigated alloys, the electrochemical performance of Ti-26Nb-4Zr-3Mn and Ti-26Nb-4Zr-5Mn have also been analyzed in this work. The electrochemical measurements show that both alloys have almost similar corrosion potential and corrosion current density in simulated body fluid, i.e., −0.45 V and 0.838 nA/cm^2 for Ti-26Nb-4Zr-3Mn, −0.48 V and 0.839 nA/cm^2 for Ti-26Nb-4Zr-5Mn, respectively.

1. Introduction

The superior combination of strength, plasticity, toughness, corrosion and wear resistance makes titanium (Ti) and its alloys promising candidates for orthopedic applications [1–3]. To date, Ti-6Al-4V and commercially pure Ti (CP-Ti) have been widely applied in the field of prosthetic implants [4]. However, when used as prosthetic implants these alloys may cause two main health problems: (i) stress shielding, which occurs due to the mismatch of elastic moduli between a biomaterial implant (nearly 110 GPa) and a surrounding hard tissue (nearly 30 GPa) and (ii) cytotoxicity due to the presence of vanadium (V) and aluminium (Al) heading to neurological disorders, bone fragility and Alzheimer's disease [5–7]. So far, researchers have made rigorous endeavors to develop Ti alloys which are free from V and Al ions and simultaneously, comprising low modulus. Among Ti alloys, particularly β-type Ti alloys have been gaining popularity because of their distinctive attributes such as their enhanced strength, low elastic modulus, large plasticity and improved corrosion resistance [8–10]. Therefore, efforts are being made by researchers in order to develop improved β-Ti alloys by adding the sufficient quantities of β-stabilizers. In recent years, the number of Ti—Nb and Ti-Nb-Zr alloys such as Ti—35Nb [11], Ti—25Nb [12], Ti-22Nb-10Zr [13], Ti-20Nb-6Zr [14], Ti-20Nb-13Zr [15], Ti-13Nb-13Zr [16], Ti-28Nb-35.4Zr [17] etc. have been investigated for orthopedic applications. The Ti—Nb and Ti-Nb-Zr systems exhibit superior mechanical and corrosion behavior in terms of low modulus and high corrosion potential (e.g., Ti—35Nb exhibits a large plasticity of approximately 47% and an increased corrosion potential of −310 mV. Further, Ti-13Nb-13Zr possesses a low modulus of nearly 62 GPa and a high corrosion potential of −232 mV) [13,18]. The superior properties of Ti—Nb and Ti-Nb-Zr systems are ascribed to addition of niobium (Nb) as the primary alloying element since it possesses distinguish attributes of improved β stability, low elastic modulus and high corrosion resistance [11,19]. The addition of neutral element, i.e., zirconium (Zr) and Nb to Ti has also been shown to be

* Corresponding authors.
E-mail addresses: wang_liqiang@sjtu.edu.cn (L.Q. Wang), l.zhang@ecu.edu.au, lczhangimr@gmail.com (L.C. Zhang).

https://doi.org/10.1016/j.msec.2020.110728
Received 13 September 2019; Received in revised form 18 December 2019; Accepted 3 February 2020
Available online 03 February 2020
0928-4931/

effective in improving the β stability and reducing the elastic modulus of Ti-Nb-Zr alloys [20]. It has been reported that Nb and Zr are better biocompatible elements than V and Al [13].

In the quest for Ti alloys with low elastic modulus, the well-known strength-plasticity trade-off dilemma should also be considered carefully to achieve the high mechanical performance of newly developed Ti alloys [21]. The strength of metals and alloys are controlled by impeding dislocation movement, which can be achieved by introducing the defects in crystalline lattice [22]. The movement of dislocations is mainly impeded by interactions with (i) solute atoms, (ii) grain boundaries, (iii) other dislocations and (iv) precipitates [22]. As such, the specific strengthening mechanisms are known as solid-solution strengthening, grain-boundary strengthening, dislocation strengthening and precipitate strengthening, respectively [22]. Solid solution strengthening usually occurs when solute elements such as Mn, Fe, Cr, etc. are alloyed with the β-Ti matrix because the atomic size and shear modulus of these solute atoms have large misfits in Ti solvent [23]. This difference can produce many strain fields which interact with dislocations [23]. Therefore, the interaction between dislocations and solute atoms hinders dislocation slip during yielding [24]. Another significant mechanism to improve the strength of Ti alloys is grain refinement, which involves the interaction between dislocations and grain boundaries [25]. It is well known that a relatively smaller grain size produces a larger amount of grain boundaries. Consequently, a greater number of grain boundaries could involve the restriction of dislocation motion, which does result in enhanced strength of an alloy [25]. The dislocation-dislocation interaction impedes the dislocation movement by tangling which eventually strengthens the alloys [23]. The precipitation strengthening can be achieved by inducing a second phase in the alloys [22]. These precipitates restrict the dislocation motion which causes an increase in the strength of alloys [22]. In general, each strengthening mechanism contributes differently in enhancing strength of an alloy and therefore the investigation on individual strengthening mechanism is useful to develop an improved Ti alloy for biomedical applications. Hence, the individual contribution of strengthening mechanisms, i.e., solid-solution, grain-boundary and dislocation strengthening mechanisms is evaluated in the present work.

As reported, manganese (Mn) is a strong and low-cost β-stabilizer which possesses low cytotoxic properties, and it is an abundant element which can be used to design high-strength Ti alloys [26]. It was stated that Mn produces enhanced solid solution strengthening effect [26,27]. Technically, two factors enhance the solid solution strengthening ability of Mn as an alloying element: (i) Mn dissolution in solid solution and (ii) smaller atomic radius of Mn (0.127 nm) as compared to Ti (0.147 nm) and Nb (0.146 nm) [27]. Moreover, Mn possesses a very good osseointegration properties and it also effectively helps in the formation of natural bones and their connective tissues [28]. Pedro et.al [28] reported that Mn has much lower cytotoxicity than V. Therefore, considering the pros and cons of Ti alloys discussed above and the valuable traits of Mn as a biomaterial, Mn is alloyed with Ti-Nb-Zr systems in order to optimize the strength, plasticity and corrosion resistance of Ti alloys for biomedical applications.

Based on the points discussed above, a series of new quaternary Ti-Nb-xZr-yMn (x = 4, 7, 10 wt% and y = 3, 5 wt%) alloys were designed with an aim to attain an effective balance between plasticity and strength. The phase analysis, microstructures, compressive mechanical properties, Vickers micro-hardness indentation and strengthening mechanisms of newly designed Ti-Nb-xZr-yMn were investigated systematically. Furthermore, dislocation density has been determined to evaluate the dislocation-pinning effect of the investigated alloys. Furthermore, the corrosion behavior of Ti-26Nb-4Zr-3Mn and Ti-26Nb-4Zr-5Mn in artificial body simulated fluid (modified Hank's solution) was investigated using standard electrochemical techniques.

Table 1
The values of mean bond order ($\overline{Bo}$) and mean metal d-orbital energy level ($\overline{Md}$), and the lattice parameters (a) of β phase (a_β) estimated from XRD patterns in as-cast (a_β) and after compression testing (a_β*) and the mean grain size (D) estimated by ImageJ for all the Ti-26 wt% Nb-(4, 7, 10) wt% Zr-(3, 5) wt% Mn alloys.

Alloys	Chemical composition (wt%)	$\overline{Bo}$	$\overline{Md}$	a_β (nm)	a_β*(nm)	D (μm)
T43	Ti-26Nb-4Zr-3Mn	2.8438	2.4169	0.3275	0.3278	203 ± 32
T73	Ti-26Nb-7Zr-3Mn	2.8503	2.4255	0.3277	0.3281	245 ± 50
T103	Ti-26Nb-10Zr-3Mn	2.8570	2.4345	0.3279	0.3284	315 ± 54
T45	Ti-26Nb-4Zr-5Mn	2.8426	2.391	0.3269	0.3274	122 ± 27
T75	Ti-26Nb-7Zr-5Mn	2.8491	2.3993	0.3271	0.3277	183 ± 29
T105	Ti-26Nb-10Zr-5Mn	2.8558	2.4078	0.3276	0.3280	244 ± 45

2. Experimental methodology

2.1. Material design and preparation

The materials used in this work were a series of Ti-26Nb-xZr-yMn (x = 4, 7, 10 wt% and y = 3, 5 wt%) alloys. The nominal compositions of Ti-26Nb-4Zr-3Mn, Ti-26Nb-7Zr-3Mn, Ti-26Nb-10Zr-3Mn, Ti-26Nb-4Zr-5Mn, Ti-26Nb-7Zr-5Mn and Ti-26Nb-10Zr-5Mn are henceforth denoted as T43, T73, T103, T45, T75 and T105, respectively, whereas a series of the Ti-26Nb-xZr-yMn alloys is denoted as the TNZM alloys from now onwards. The TNZM alloys and their elemental concentrations were theoretically designed using DV-Xα cluster design strategy. The mean values of bond order ($\overline{Bo}$) and metal d-orbital energy level ($\overline{Md}$) for the designed alloys are shown in Table 1. The $\overline{Bo}$ and $\overline{Md}$ values were designed with an objective to achieve the fully stabilized β phase based on the phase stability map suggested by Abdel-Hady et al. [29]. The theoretically designed compositions of newly developed alloys were produced through a cold crucible levitation melting (CCLM) technique under a high-purity Ti-gettered argon atmosphere. In this work, 99.9% pure alloying elements were used as raw metals in the casting process to produce Ti-26 wt% Nb-xZr-yMn (x = 4, 7, 10 wt% and y = 3, 5 wt%) alloys. The CCLM technique was used for production of alloys to eliminate some of the problems such as inhomogeneity in producing alloys comprising elements with different melting points and specific gravities involved in the production of β Ti alloys [28]. The CCLM furnace was comprised of water-cooled crucible which was integrated with copper segments. The crucible was surrounded by spark coils which were connected to frequency inverter power supply. After completion of melting and subsequent mixing of raw metals, the electric supply was switched off. Afterwards, the solidification of molten metals into an ingot was performed with in the water-cooled crucible. Subsequently, the ingots of all the TNZM alloys were remelted and flipped five times to augment their chemical homogeneity. The cylindrical rods with 5.4 mm in diameter were extracted from the center of ingots using a spark machining for all types of investigations employed in this work to avoid any characteristic changes that may be caused due to the cooling effect.

2.2. Material characterization

Prior to the material characterizations, the button-shaped flakes of 5.4 mm diameter were grounded and polished using SiC papers up to 4000 grits and colloidal SiO_2 on a Struers MD-chem polishing pad, respectively, following the standard metallographic procedures. Subsequently, the specimens were etched by a Kroll's etchant (2 vol% HF, 6 vol% HNO_3 and 92 vol% H_2O). For microstructural characterizations, high resolution scanning electron microscopy (SEM) was performed on the TNZM alloys using a FEI Helios Nanolab G3 CX DualBeam scanning electron microscope. Furthermore, quantitative analysis was conducted through an energy dispersive X-ray

spectroscopy (EDX) detector equipped in the aforementioned microscope. The constituent phases of the TNZM alloys were analyzed by X-ray diffraction (XRD) using a PANalytical EMPYREAN diffractometer with a cobalt (λ = 0.1789 nm) source for all the TNZM alloys before and after mechanical compression testing. The phase information for all the TNZM alloys was obtained from JCPDS powder diffraction files using International Centre for Diffraction Data (ICDD). The values of lattice parameter (a) for the TNZM alloys were estimated for the as-cast and deformed (after compression testing) TNZM alloys using Bragg's formula and Nelson-Riley's extrapolation function reported in Ref. [21, 30]. Furthermore, the values of dislocation density were determined using the XRD line broadening analysis after compression testing for all the TNZM alloys which was based on the Williamson-Smallman equation expressed as Eq. (1) [31]:

$$\rho = \frac{2\sqrt{3} \bullet s}{b \bullet d} \tag{1}$$

where ρ is dislocation density, s is micro-strain, d is crystallite size and b is Burgers vector. The value of b is estimated using $b = < 111 > a/2$ [32]. The values of d and s were estimated using the expression proposed by Williamson-Hall based on the XRD peak broadening analysis as presented in Eq. (2) [33].

$$\delta_{st} cos\theta = \frac{C\lambda}{D} + (4sin\theta) \tag{2}$$

where C is a constant (~ 0.9), λ is the wavelength of Co radiation and δ_{st} is structural broadening. The δ_{st} comprises of the micro-strain broadening (δ_s) and the crystallite size broadening (δ_d). Nonetheless, the total broadening (δ_o) consists of the δ_{st} and the instrumental broadening (δ_i) as shown in Eq. (3) [34].

$$\delta_o = \delta_{st} + \delta_i \tag{3}$$

where δ_o is total broadening, δ_{st} is structural broadening and δ_i is instrumentational broadening. The Bragg's diffraction peaks were fitted by means of the Voigt function using a Highscore Plus software from which θ and δ_{st} for each peak were obtained. In this work, the values of δ_{st} were directly obtained from HighScore Plus software supplied by the manufacturer of diffractometer which provides the value of δ_{st} after subtracting the value of δ_i. The slope and y-intercept of linear profile fit of the δ_{st}cosθ–4sinθ plot was used to estimate the values of s and d, respectively.

The mechanical testing of the TNZM alloys including compression and hardness testing was performed using an Instron 5982 electromechanical universal testing system and Zwick Roell Vickers hardness testing machine, respectively. The mechanical compression tests were conducted at a cross head speed of 0.1 mm/min on cylindrical specimens and were prepared according to the ASTM E9 standard (considering the ratio of length to diameter of a specimen between 1.5 and 2). Accordingly, the two end surfaces of the cylindrical specimens were ground to flatten surfaces of each TNZM alloy. The average values of three measurements were considered for all compressive mechanical properties. The well-known 0.2% strain offset method was applied to estimate the yield strength from compressive stress-strain curves. The values of plastic strain and maximum compressive strength were obtained at 100 kN from engineering stress-strain curves of the TNZM alloys. The values of compressive true stress (σ_t) and true strain (ε_t) for each TNZM alloy were obtained using the expressions reported in Ref. [35] for compression tests. The corresponding value of σ_t at ε_t = 1 mm/mm was considered as the value of strength coefficient for each TNZM alloy. Furthermore, strain hardening indices (n_1 & n_2) were also evaluated using lnε_t-lnσ_t plots (drawn for the plastic regions of the TNZM alloys). The values of lnε_t versus lnσ_t were plotted considering the plastic zone to obtain the value of n_1 & n_2 for each TNZM alloy. Afterwards, the values of first strain hardening stage (n_1) which displays the elastic-plastic deformation were obtained from the slope of plastic yielding region, whereas the values of second strain hardening stage (n_2) which shows the complete plastic deformation were obtained from the slope of complete plastic deformation region. The microhardness tests were carried out at 5 kgf load with 30 s dwell time. The average of at least 12 indentations was taken and the mean hardness value was considered for each TNZM alloy.

Table 2
The chemical constituents of modified Hank's solution.

Chemical agent	Constituents (g/L)	Chemical agent	Constituents (g/L)
$NaHCO_3$	0.350	NaCl	8.000
Na_2HPO_4	0.048	KCl	0.400
KH_2PO4	0.060	C_6H12O_6	1.000
$CaCl_2$	0.140	$C_{19}H_{14}O_5SNa$	0.011
$MgSO_4$	0.098	–	–

2.3. Electrochemical measurements

The electrochemical measurements of T43 and T45 were carried out by means of PARASTAT 2273 potentiostat using a three-electrode system connected to a Luggin capillary bridge. The circular rods of 5.3 mm diameter were used for the electrochemical measurements of T43 and T45 alloys. The polished test specimens (i.e., T43 and T45) with an exposed base area of 0.22 cm^2, a platinum net and a saturated calomel electrode which serves as working, counter and reference electrodes, respectively were included in the three-electrode system. The electrochemical measurements were conducted in artificially aerated body simulated fluid (modified Hank's solution) at normal body temperature of 37 °C and the pH of 7.4 close to human body fluid was maintained. The composition of simulated body fluid (modified Hank's solution) is presented in Table 2. The open circuit potential (OCP) measurements were conducted for 1 h to obtain a stable state for each tested specimen. The potentiodynamic polarization curves of T43 and T45 specimens were obtained over the scan range of −0.6 V to +1.8 V (Vs OCP) at a sweep scan rate of 1 mV/s. In the meantime, an electrochemical impedance spectroscopy (EIS) test was acquired over the frequency range of 0.1 Hz to 100 kHz at an alternating current amplitude of 10 mV. In order to estimate the corrosion current density (i_{corr}) and corrosion potential (E_{corr}), the Tafel extrapolation was performed on the anodic and cathodic regions of potentiodynamic polarization curves of each tested specimens using an Origin 8.5 fitting software. All the measurements were repeated at least three times to ensure the accuracy of the data. Moreover, the SEM and EDX analysis were performed in order to confirm the formation of oxides film on the surface of T43 and T45 specimens after 1 h immersion time in Hank's solution.

3. Results and discussion

The chemical compositions by EDX quantitative analysis for all the TNZM alloys are summarized in Table 3. The chemical compositions of the produced alloys are found to be approximately identical with the theoretically designed compositions.

Table 3
The quantitative analysis performed by means of EDX for all the Ti-26 wt% Nb-(4, 7, 10) wt% Zr-(3, 5) wt% Mn alloys.

Alloys	Chemical composition (wt %)	Ti (wt %)	Nb (wt %)	Zr (wt %)	Mn (wt %)
T43	Ti-26Nb-4Zr-3Mn	Bal.	26.7	4.0	3.1
T73	Ti-26Nb-7Zr-3Mn	Bal.	25.4	7.2	2.9
T103	Ti-26Nb-10Zr-3Mn	Bal.	26.1	9.7	2.8
T45	Ti-26Nb-4Zr-5Mn	Bal.	26.0	3.8	4.8
T75	Ti-26Nb-7Zr-5Mn	Bal.	27.2	6.7	4.7
T105	Ti-26Nb-10Zr-5Mn	Bal.	27.3	9.7	4.9

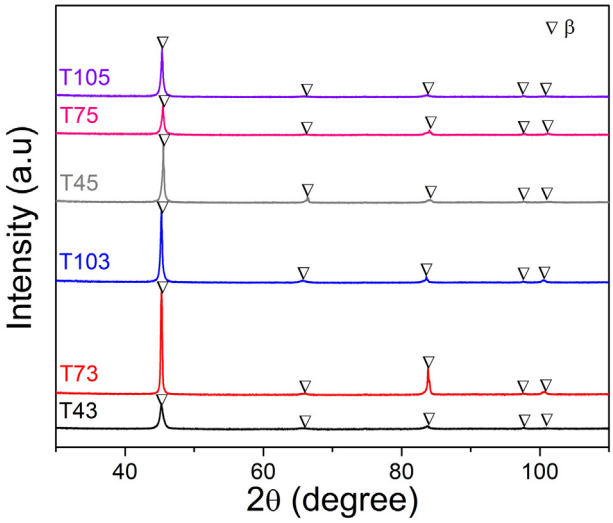

Fig. 1. XRD profiles of the Ti-26Nb-xZr-yMn (x = 4, 7, 10 wt% and y = 3, 5 wt %) alloys (The alloys are named in the Txy format).

3.1. Phase and microstructure characterizations

Fig. 1 shows the XRD profiles of all the TNZM alloys. All the TNZM alloys show the peaks related to body-centred cubic (bcc) β phase (PDF card no.: 00-044-1288 and 01-071-9942). The diffraction peaks slightly shift towards a higher 2θ angle when augmenting the amount of Mn in the TNZM alloys. This phenomenon occurs because of the addition of Mn which possesses the smaller atomic radius than Ti. Furthermore, the a of bcc β phase (a_β) in as-cast condition for the TNZM alloys are presented in Table 1. The decreasing trend of a_β is apparent while increasing the amount of Mn in the TNZM alloys. The decreasing trend in the values of a_β occurs due to replacing Ti by Mn comprising smaller atomic radius than Ti [36]. Whereas, the increasing trend in the values of a_β can be observed by increasing the amount of Zr in the TNZM alloys because Zr has a larger atomic radius compared to Ti [37]. In this work, the XRD profile of each alloy was acquired at slow scan speed of 0.011°/s and a step size of 0.013°. In XRD profiles of the investigated alloys, the peaks associated with miller indices 001, 111, 002, 112 of ω phase are not detected with Co-kα radiation source (Space group: P6/mmm, PDF card no: 00–051-0631) [38]. Therefore, ω phase is not expected in all the TNZM alloys.

The microstructural topographies of all the TNZM alloys are presented in Fig. 2. The equiaxed bcc β grains with elongated grain boundaries can be observed for all the TNZM alloys. Furthermore, the dendritic substructure is obvious in the β grains of all the TNZM alloys which typically forms during solidification process after casting. The mean grain size for each TNZM alloy estimated using an ImageJ software is shown in Table 1. Among the TNZM alloys, the T103 displays the largest mean grain size of 315 ± 54 μm, whereas T54 shows smallest mean grain size of 122 ± 27 μm. It is noted that the mean grain size of the TNZM alloys decreases as the amount of Mn as a solute atom increases. The reduction in grain size of the TNZM alloys occurs due to the addition of Mn. In general, Mn comprises high growth-restriction factor when alloy to Ti and therefore, the addition of Mn in the TNZM alloys leads to a grain refinement [39]. By contrast, grain size increases when increasing the amount of Zr in the TNZM alloys. A similar trend has been reported in the previous studies [36,40]. The phase and microstructural characterizations indicate that all the TNZM alloys are comprised of a monolithic β phase. It has been reported in previous studies that the addition of 30 wt% or high quantities of Nb in Ti−Nb binary alloys can result in monolithic β phase [41]. In this work, Mn and Zr are added with 26% of Nb to compensate towards the stabilization of a monolithic β phase in all the TNZM alloys.

3.2. Mechanical characterizations

It is well known that the microstructure and phase characterization of an alloy greatly influence their mechanical properties [42,43]. The newly designed TNZM alloys were subjected to mechanical compression testing in order to demonstrate its rudimentary mechanical characterizations. As a matter of fact, the bones and surrounding hard tissues are primarily subjected to compressive loads; therefore, the compression testing has been carried out in this work [44]. Fig. 3a displays compressive engineering stress strain curves for all the TNZM alloys. Moreover, the properties of true stress-strain curves of polycrystalline materials remain analogous in compression and in tension [35,45]. Therefore, the compressive true stress-strain curves for all the TNZM alloys have also been presented in Fig. 3b. All the TNZM alloys exhibit a significant plastic deformation in mechanical compression testing. The engineering stress-strain curves (Fig. 3a) of the TNZM alloys are comprised of mainly three stages, i.e., elastic stage, plateau stage and densification stage [46]. According to Gibson-Ashby's model for compressive stress-strain curves, the unit cell wall bending, the collapse of the unit cell and the continuous load applied to strengthen the completely collapsed unit cells remain responsible for the elastic stage, the plateau stage and the densification stage, respectively [8]. Notably, all the TNZM alloys do not display a fracture during the compression tests within the load capacity of 100 kN. The values of engineering maximum compressive strength and plastic strain presented in Table 4 were obtained at 100 kN for all the TNZM alloys. All the TNZM alloys demonstrate engineering plasticity of ~80% and engineering maximum strength of ~5 GPa due to the strong β-phase stability found in all the TNZM alloys [19]. The true stress-strain curves (Fig. 3b) display significant amount of plasticity and strength within the load capacity of 100 kN. An oscillating effect can be noted in plastic region of true stress-strain curves that shows a softening behavior which occur due to stress relaxation [45]. The values of true maximum strength and plastic strain presented in Table 5 were obtained at 100 kN for all the TNZM alloys. All the TNZM alloys display significant true plasticity of ~160% and true maximum strength of ~950 MPa. In general, the instantaneous cross-sectional area of a specimen increases when a material undergoes the deformation in the plastic region during compression testing. Therefore, engineering strain remains lower than true strain and contrastingly, engineering stress remains higher than engineering strain [35,45]. The analogous behavior can be observed for true strain with engineering strain and true stress with engineering strain values of the TNZM alloys. Moreover, the TNZM alloys display moderate hardness values in the range of 200–250 HV (Table 4). The values of hardness increase upon increasing the amount of Mn in the TNZM alloys. By contrast, the value of hardness decreases upon increasing the amount of Zr in the TNZM alloys.

In order to calculate the dislocation density as well as to confirm the formation of any stress induced martensitic transformation (SIMT) during deformation, the XRD analyses have been carried out on a deformed specimen (after compression testing) of all the TNZM alloys. It is evident in Fig. 4 that all the investigated alloys show only a single bcc β-phase even after compression testing and the evidence of peaks related to martensitic phases in the XRD spectra are not found. This suggests that the SIMT does not occur during the deformation of all the TNZM alloys. The values of a_β* for all the TNZM samples after compression testing presented in Table 1 followed a similar trend like a_β, however, the values of a_β* are increased in comparison to the values of a_β due to the lattice distortion that occurs when a material undergoes a compression testing or a rolling operation [35,47].

3.3. Strengthening mechanism

The strengthening mechanism for monolithic β phase Ti alloys has been recently modelled by Zhao et al. [48] through the integration effect of solid-solution hardening, grain-boundary hardening and

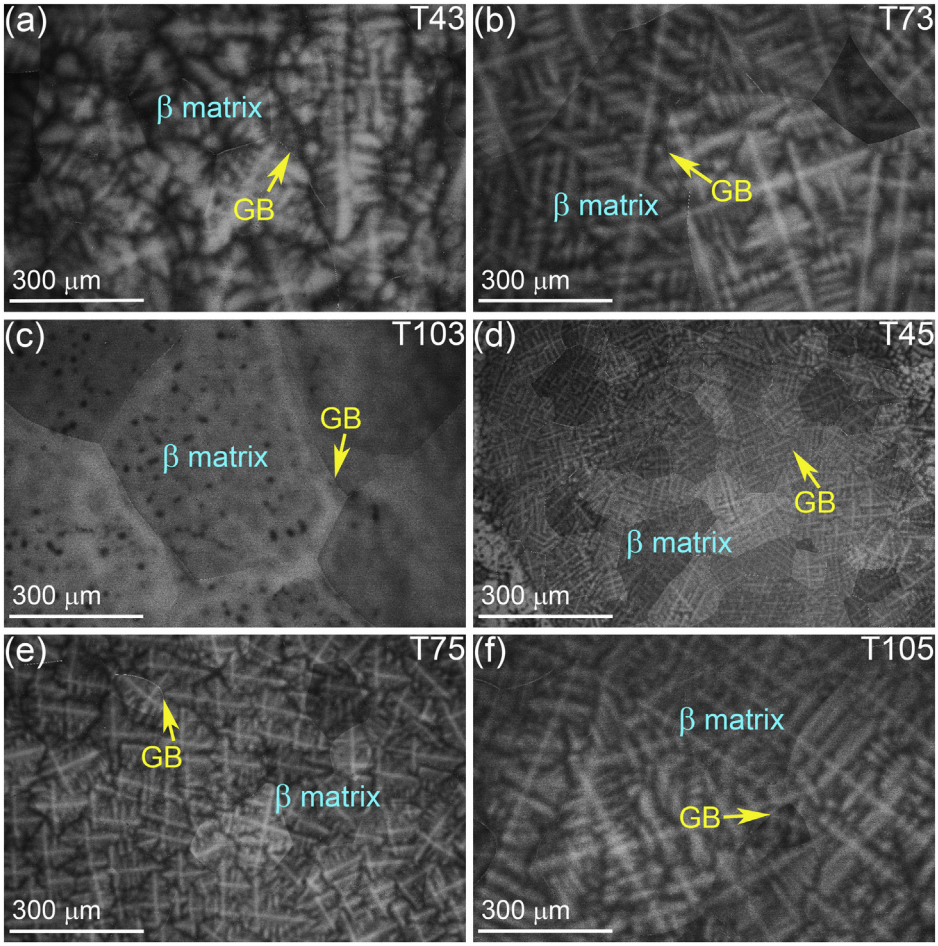

Fig. 2. The backscattered SEM microstructural features of the Ti-26Nb-xZr-yMn (x = 4, 7, 10 wt% and y = 3, 5 wt%) alloys (The alloys are named in Txy format). Note that grain boundary is labelled as GB.

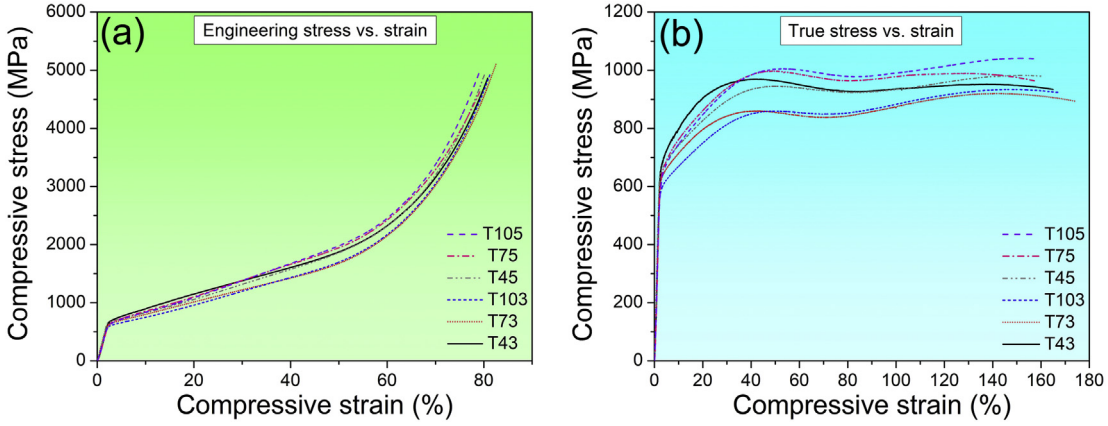

Fig. 3. The (a) engineering and (b) true stress-strain curves of the Ti-26Nb-xZr-yMn (x = 4, 7, 10 wt% and y = 3, 5 wt%) alloys (The alloys are named in Txy format).

dislocation hardening. The solid solution hardening is usually defined by the elastic misfit (η) and lattice parameter misfit (γ) between the solvent and solute atoms [23,49]. The effect of solid solution strengthening was first studied by Fleisher et al. [50], in which the effect of isolated solute atoms was determined in the crystal structure of the solvent. Thus, the isolated solute atoms hinder the dislocation movement. This approach was further extended by Gypen et al. [51] and Toda-Caraballo et al. [50] to approximate the solid solution hardening in multi component alloys. The solid solution hardening in multi-component alloys can be expressed using Eq. (4) [50]:

$$\sigma_{ss} = \left(\sum_i B_i^{3/2} X_i \right)^{2/3} \quad (4)$$

where σ_{ss} is yield strength component produced due to solid solution hardening, B_i is solid solution strengthening co-efficient which depends on η and γ, and X_i is fraction of solute atom in an alloy. The values of B_i for the alloying elements Nb, Zr and Mn in Ti alloys were taken as 71, 1201, 1485 MPa.at.$^{-2/3}$, respectively [48]. Conventionally, the grain-boundary strengthening increases the strength of an alloy through grain-boundary refinement and therefore, it is also known as grain

Table 4
The compressive engineering mechanical properties such as yield strength ($\sigma_{0.2}$), plastic strain (ε_p) and maximum strength (σ_{max}) along with hardness (H) obtained for all the Ti-26 wt% Nb-(4, 7, 10) wt% Zr-(3, 5) wt% Mn alloys.

Alloys	Chemical composition (wt%)	$\sigma_{0.2}$ (MPa)	ε_p (%)	σ_{max} (GPa)	H (HV)
T43	Ti-26Nb-3Mn-4Zr	591 ± 18	79.2 ± 0.5	4.91 ± 0.12	225 ± 5
T73	Ti-26Nb-3Mn-7Zr	557 ± 6	80.4 ± 0.4	5.13 ± 0.21	219 ± 2
T103	Ti-26Nb-3Mn-10Zr	451 ± 19	80.0 ± 0.4	4.94 ± 0.35	207 ± 5
T45	Ti-26Nb-5Mn-4Zr	609 ± 18	78.9 ± 0.7	4.91 ± 0.21	242 ± 5
T75	Ti-26Nb-5Mn-7Zr	571 ± 3	77.7 ± 0.5	4.89 ± 0.30	236 ± 4
T105	Ti-26Nb-5Mn-10Zr	488 ± 19	77.9 ± 0.3	4.90 ± 0.15	228 ± 4

Table 5
The compressive true mechanical properties such as plastic strain ($\varepsilon_{p,\ T}$), maximum strength ($\sigma_{max,\ T}$) and strength co-efficient (K) obtained for all the Ti-26 wt% Nb-(4, 7, 10) wt% Zr-(3, 5) wt% Mn alloys.

Alloys	Chemical composition (wt%)	$\varepsilon_{p,\ T}$ (%)	$\sigma_{max,\ T}$ (MPa)	K (MPa)
T43	Ti-26Nb-3Mn-4Zr	163 ± 2	923 ± 54	902 ± 18
T73	Ti-26Nb-3Mn-7Zr	166 ± 7	935 ± 42	889 ± 20
T103	Ti-26Nb-3Mn-10Zr	168 ± 2	929 ± 16	865 ± 26
T45	Ti-26Nb-5Mn-4Zr	162 ± 3	964 ± 39	1000 ± 19
T75	Ti-26Nb-5Mn-7Zr	157 ± 2	961 ± 23	974 ± 15
T105	Ti-26Nb-5Mn-10Zr	157 ± 2	968 ± 23	921 ± 24

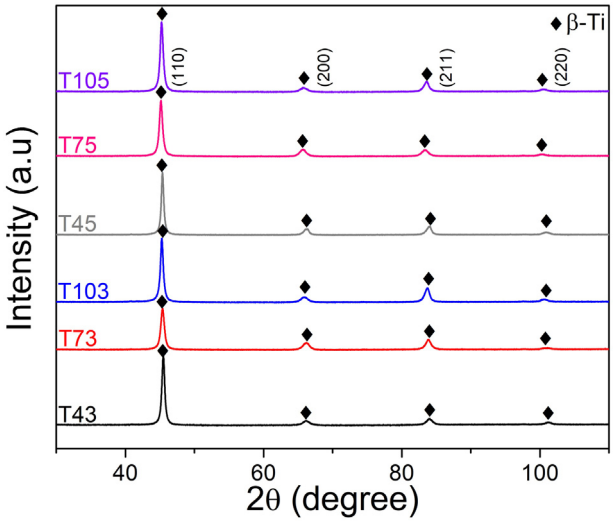

Fig. 4. XRD spectra of the Ti-26Nb-xZr-yMn (x = 4, 7, 10 wt% and y = 3, 5 wt %) alloys after compression testing (The alloys are named in the Txy format).

refinement strengthening [52]. It has been established that the small sized grains provide a greater number of grain boundaries which could immensely hinder the dislocations movement [25]. The grain-boundary strengthening in an alloy can be estimated using the classical Hall-Petch expression using Eq. (5) [52]:

$$\sigma_{gb} = \sigma_o + \frac{k_Y}{\sqrt{D}} \tag{5}$$

where σ_{gb} is yield strength component produced due to grain refinement, σ_o is friction stress, k_Y is Hall-Petch constant and D is mean grain size. The values of k_Y were derived using the expression Eq. (6):

$$k_y = k_{Ti} + \sum_i k_i X_i \tag{6}$$

where k_{Ti} and k_i are Hall-patch constants for pure Ti and alloying elements, respectively. The value k_{Ti} for pure Ti is 0.75 MPa·m$^{1/2}$ and the values of k_i for Nb, Zr and Mn in Ti alloys were taken as 1.05, 0.28, 0.06 MPa·m$^{1/2}$, respectively [52–54]. Moreover, the dislocation strengthening occurs when two dislocations gliding on the different slip planes cross each other and consequently, their total energy reduces and a new junction forms as a third dislocation segment [55]. This dislocation junction is immobilized and it impedes the other dislocations movement. The critically resolved shear stress (τ) needs to break this junction so that the dislocations cross each other based on a relationship Eq. (7):

$$\tau \propto \mu b/l \tag{7}$$

where μ is shear modulus, b is burgers vector and l is length between the interesting obstacles and the mean value of length (l_m) is related to dislocation density according to a relationship: $l_m \propto 1/\sqrt{\rho}$ [55]. This phenomenon leads to the famous Bailey-Hirsch expression demonstrating the dislocation strengthening as Eq. (8) [56]:

$$\sigma_\rho = \alpha M \mu b \sqrt{\rho} \tag{8}$$

where σ_ρ is yield strength component produced due to dislocation strengthening, α is mean junction strength (0.3), M is Taylor factor (2.8), μ is shear modulus for Ti (45 GPa), b is Burgers vector and ρ is dislocation density of an alloy [23,48]. The theoretical yield stress for β-type Ti alloys operating with slip dominated mechanism can be predicted using the following model that can be expressed as Eq. (9) [48].

$$\sigma_Y = \sigma_{Ti} + \alpha M \mu b \sqrt{\rho} + \left(\sum_i B_i^{3/2} X_i\right)^{2/3} + \frac{k_{Ti} + \sum_i k_i X_i}{\sqrt{D}} \tag{9}$$

where σ_{Ti} is slip activation critical stress for Ti. Considering the solid-solution, grain-boundary and dislocation strengthening mechanisms, the contribution of each strengthening mechanism estimated using the corresponding equations described above is presented in Fig. 5 for each TNZM alloy. It can be noted in Fig. 5 that the grain-boundary

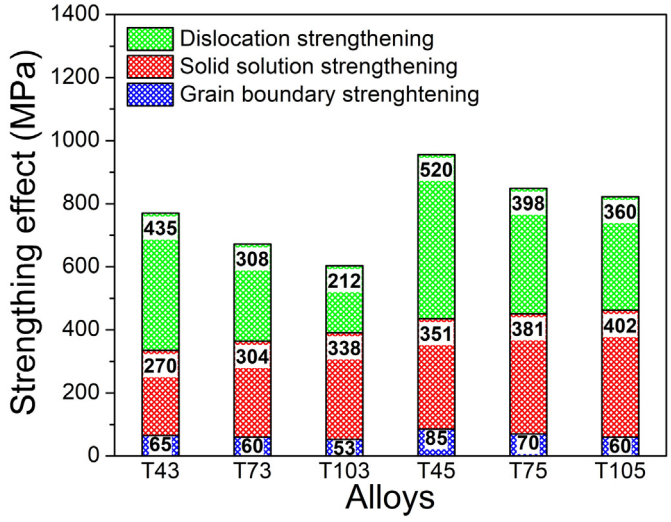

Fig. 5. The estimated strengthening contributions of the dislocation, solid-solution and grain-boundary strengthening mechanisms in yield strength of the Ti-26Nb-xZr-yMn (x = 4, 7, 10 wt% and y = 3, 5 wt%) alloys (The alloys are named in Txy format).

strengthening contributes the least in strengthening the TNZM alloys. By contrast, the dislocation and solid solution strengthening mechanisms are the main contributors in enhancing the strength of the TNZM alloys. Notably, the trend of σ_ρ is directly proportional to dislocation density of the TNZM alloys, whereas both Mn and Zr are producing the solid solution strengthening effect and increases the σ_{ss} in the TNZM alloys because of their high values of B_i in Ti alloys.

Nonetheless, Fig. 5 demonstrates the greater contribution of dislocation and solid-solution strengthening mechanisms as compared to grain-boundary strengthening because grain- boundary strengthening correlates with the grain size. All the TNZM alloys comprise large grain size (> 120 μm). Therefore, the number of grain boundaries remains less and as a result, the contribution of grain-boundary strengthening remains less as compared to dislocation and solid-solution strengthening mechanisms. Moreover, dislocation strengthening can occur inside the grains as well as at the grain boundaries due to interaction of multiple dislocations, whereas the strengthening effect produced due to solid solution strengthening remains directly proportional to the amount of Zr and Mn added in the TNZM alloys, which can be evidently seen in Fig. 5. This demonstrates that the interaction of dislocations should have occurred extensively and therefore, the interaction of dislocations produces the greater amount of strengthening.

The values of measured true yield strength and dislocation density for all the TNZM alloys are presented in Fig. 6. It can be noted that measured engineering yield strength and measured true yield strength followed an identical trend. Therefore, from now onwards the values of true yield strength have been used in subsequent discussion. It can be noted in Fig. 6 the measured true yield strength displays an increasing trend upon the addition of Mn as a solute atom because Mn has relatively higher values of η and γ [27,48]. Consequently, Mn produces a strong solid solution strengthening effect in the TNZM alloys. The direct relationship between true yield strength and dislocation density has been demonstrated by the Bailey-Hirsch relationship in Eq. (8). Accordingly, it can be noted in Fig. 6 that the dislocation density is directly proportional to the true yield strength for all the TNZM alloys. By contrast, the Hall-Petch relationship demonstrates the inverse relationship between the measured true yield strength and mean grain size of an alloy [52]. Hence, the measured true yield strength varies with mean grain size (Table 1) for all the TNZM alloys. Thus, the measured true yield strength of all the TNZM alloys are influenced by the combined effects of solid-solution, grain-boundary and dislocation strengthening. Notably, T45 possesses the highest measured true yield strength (654 ± 12 MPa) among all the TNZM alloys.

As shown in Fig. 3a, the strain hardening ability of all the TNZM alloys is apparent. The strain hardening ability is generally characterized in terms of either the strain hardening rate or the strain hardening index [57]. In this work, to characterize the strain hardening ability of the TNZM alloys in the plastic region, the strain hardening index which symbolizes the resistance to plastic deformation [58] can be evaluated by using a classical Holloman expression using Eq. (10) [59].

$$\sigma_t = K\varepsilon_t^{\,n} \tag{10}$$

where σ_t is true stress, ε_t is true strain and K is strength coefficient of a material. The material demonstrates the perfect elastic fracture when the value of strain hardening index is equal to 1, whereas it displays a complete plastic deformation when the value of strain hardening index is equal to 0 [58]. To evaluate the values of n_1 & n_2 for the TNZM alloys, Eq. (10) is rearranged and rewritten as Eq. (11) [58].

$$ln\,\sigma_t = lnK + nln\varepsilon_t \tag{11}$$

By using Eq. (11), the ln ε_t-lnσ_t plots for all the TNZM alloys are presented in Fig. 7. It can be noted in Fig. 7a–f that the strain hardening is comprised of two stages. The n_1 displays the elastic-plastic deformation, whereas the n_2 shows the complete plastic deformation [58]. All the TNZM alloys exhibit the high n_1 and low n_2 values in the range of 0.428 ± 0.01 to 0.542 ± 0.01 and 0.125 ± 0.005 to 0.090 ± 0.006, respectively, which demonstrate their enhanced strain hardening behavior and good work formability. The values of n_1 & n_2 for the TNZM alloys rise upon increase in the Zr content, whereas the values of n_1 & n_2 demonstrate a decreasing trend upon increase in the Mn content. Similar results of strain hardening behavior have been reported in the previous studies [60,61]. The decreasing trend of the values of n_1 & n_2 is associated with an increase in dislocation density of the TNZM alloys [57]. Moreover, it has also been reported in previous studies that the strain hardening index of a material increases with increasing mean grain size up to a certain extent [62]. By contrast, strain hardening index decreases with increasing mean grain size when the amount of second phase is precipitated in an alloy [62]. The strain hardening index and mean grain size can be correlated by using the Morrison model as follows as presented in Eq. (12) [63]:

$$n = \frac{5}{(10 + D^{-1/2})} \tag{12}$$

where n is strain hardening index and D is mean grain size. In the present wok, all the TNZM alloys are comprised of a single phase. Therefore, it is noted that the values of n_1 & n_2 (Figs. 7a–f) are directly proportional to mean grain size (Table 1) for all the TNZM alloys. Furthermore, the values of strength coefficient presented in Table 5 follow the classical Hall-Petch relationship [64] as these values decrease with increasing values of n_1 & n_2 for all the TNZM alloys. The values of n_1 & n_2 for all the TNZM alloys demonstrate the high strain hardening ability and therefore, all of the TNZM alloys exhibit a significant plasticity and enhanced β phase stability [21,65]. In conclusion to mechanical characterization and strengthening mechanisms for the TNZM alloys, T45 and T43 exhibit higher yield strength and significant strain hardening capability among all the TNZM alloys.

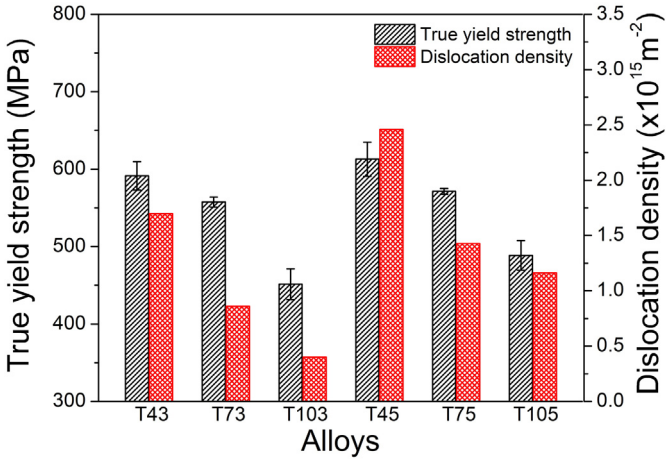

Fig. 6. True yield strength and dislocation density of the Ti-26Nb-xZr-yMn (x = 4, 7, 10 wt% and y = 3, 5 wt%) alloys (The alloys are named in Txy format).

3.4. Electrochemical performance

It has been stated that any biomaterial used for orthopedic implant application should have enhanced electrochemical performance in the human body environment [13]. It has also been documented in the literature that the Ti-Nb-Zr system demonstrates excellent corrosion resistance with any amount of alloying elements as compared to Ti-6Al-4V in any artificial human body environment and for any immersion time for electrochemical analysis [13]. The high corrosion resistance of the Ti-Nb-Zr system is ascribed to quick formation of oxide film (i.e., Ti oxide and Nb oxide) on the surface of material [13,18]. Notably, these layers have capability to self-repair any film damages, which in turn resists the additional corrosion in the material [18]. Among the all the

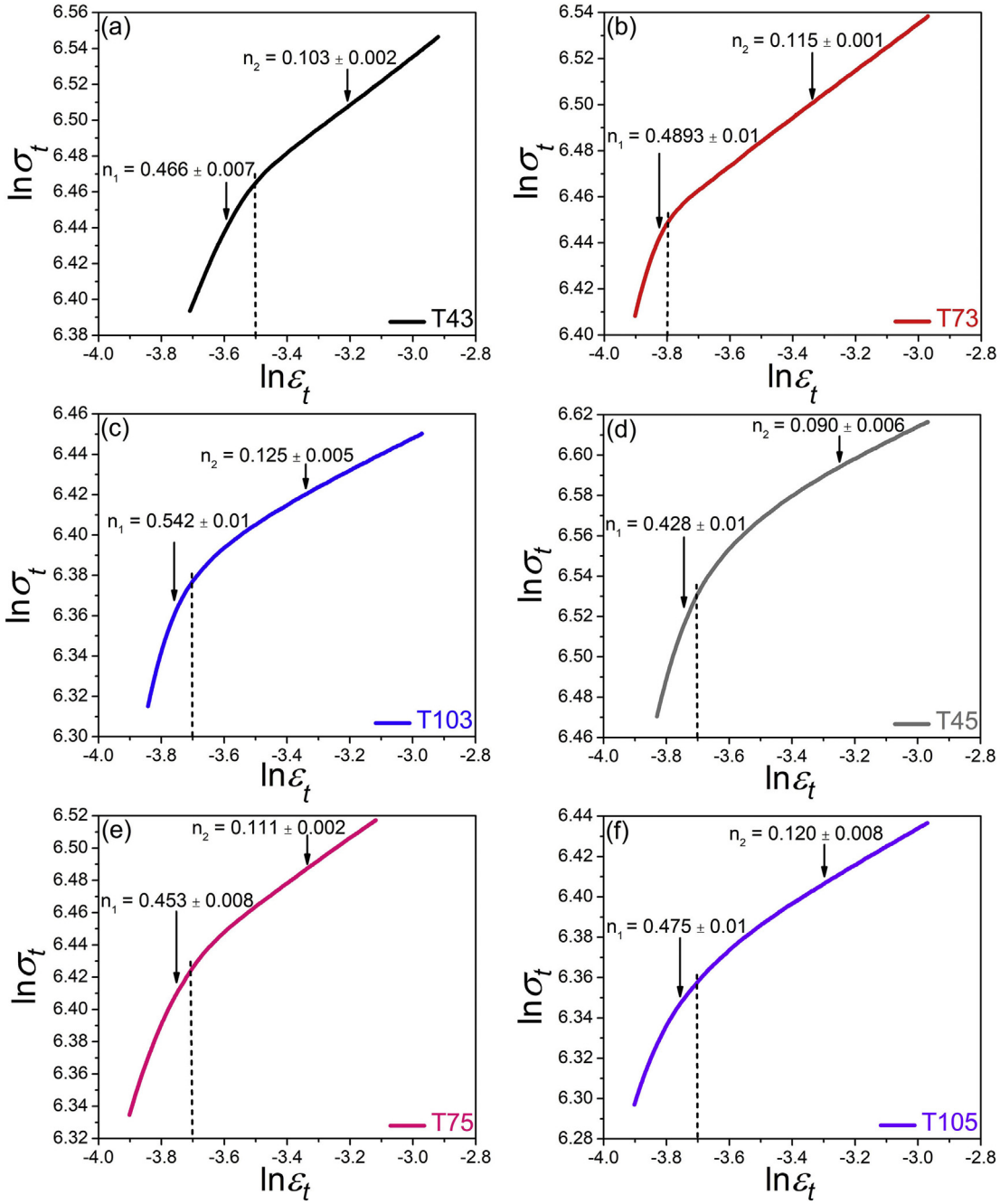

Fig. 7. Relationship between $\ln\sigma_t$ and $\ln\varepsilon_t$ for the Ti-26Nb-xZr-yMn (x = 4, 7, 10 wt% and y = 3, 5 wt%) alloys (The alloys are named in Txy format).

TNZM alloys, T43 and T45 exhibit superior mechanical properties. Therefore, the electrochemical analyses were performed for only T43 and T45 among the investigated TNZM alloys. The OCP curves for T43 and T45 are presented in Fig. 8a. The OCP curves display a slight fluctuation during the preliminary phase of the test. The fluctuating behavior is ascribed to electron movement occurred between the material surface and the simulated body fluid until the equilibrium potential attained for both sides [66]. It can be noted in Fig. 8a that both alloys attain a more positive and a stable state after few initial minutes; this trend attributes to the rapid development of oxide layer on the surface of alloys [4]. In order to better characterize the strength of the developed Ti and Nb oxide layers, potentiodynamic polarization curves are obtained in modified Hank's solution for T43 and T45 alloys and presented in Fig. 8b. The corrosion kinetics parameters, i.e. E_{corr} and i_{corr}, are obtained from the Tafel region of the potentiodynamic polarization curves. In the present work, the E_{corr} values of T43 and T45 are −0.45 and −0.48 V, respectively. The relatively positive values of E_{corr} for T43 and T45 alloys demonstrate their better corrosion resistance than the as-cast CP-Ti, i.e., −0.58 V [18]. In general, according to the concept of electrochemistry, the high value of E_{corr} and the low value of i_{corr} are the indicators for good corrosion resistance of a material [4,67]. The reported value of i_{corr} in this work for T43 and T45 are 0.838 and 0.839 nA/cm^2, respectively. Both the alloys exhibit lower i_{corr} value than the as-cast Ti-6Al-4V, i.e., 1.037 nA/cm^2 [4]. Thus, the investigated T43 and T45 alloys demonstrate a better corrosion resistance than CP-Ti and Ti-6Al-4V. Furthermore, the EIS study was carried out on the T43 and T45 alloys to illustrate the nature of formed passive oxide layer. The characterization of electron movement resistance can usually be performed by EIS Nyquist curve. The extent of semi-circular arc radius on EIS Nyquist plot is directly proportional to

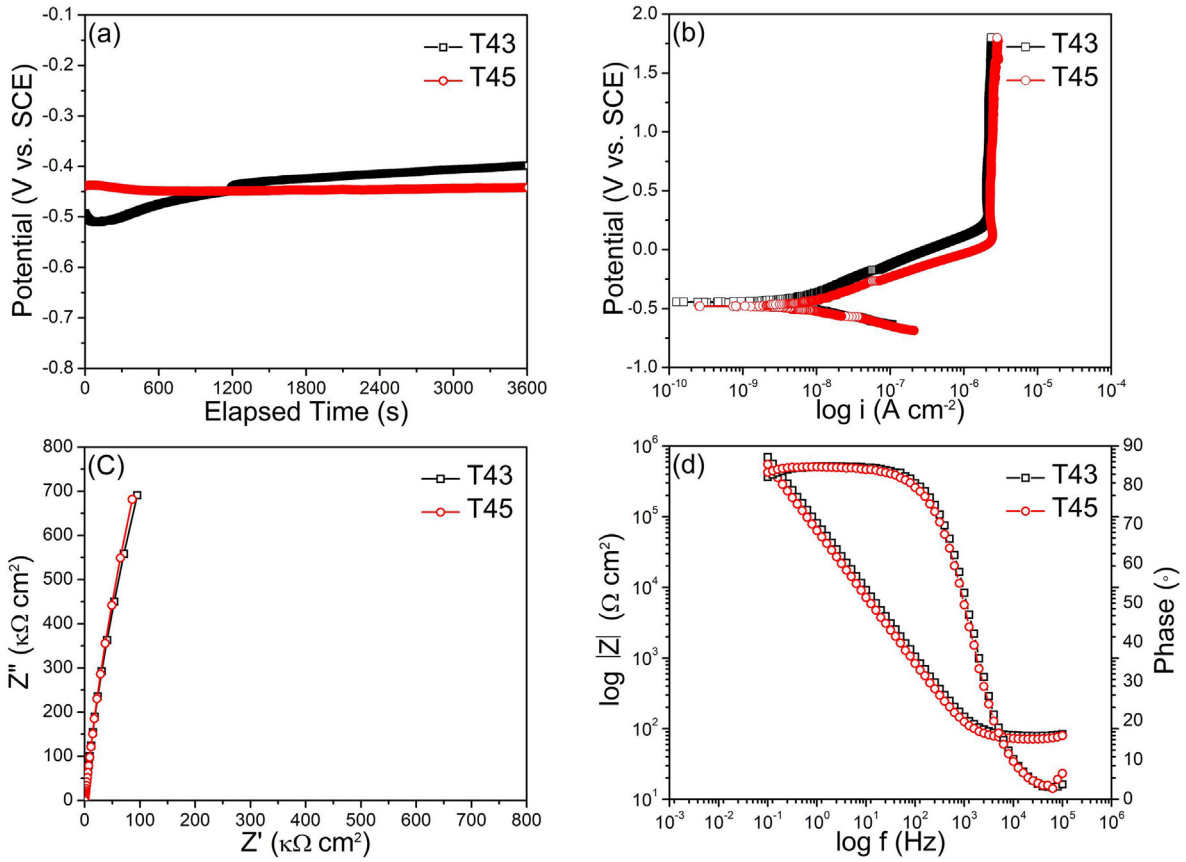

Fig. 8. Results of the electrochemical tests for the T43 and T45 alloys in modified Hank's solution at a pH value of 7.4 at room temperature. (a) Open circuit potential curves vs. time (b) Potentiodynamic polarization curves. EIS results in the form of (c) Nyquist plots and (d) Bode plots.

the corrosion resistance of a material [67]. The radius of a semi-circular arc for T43 is somewhat higher than T45, as presented in Fig. 8c which demonstrates that the passive oxide film of T43 has better polarization resistance on the surface [66]. The Bode impedance plot and the Bode phase plot are presented in Fig. 8d. The Bode impedance plot displays two distinct phases: (i) the flat phase in the frequency range of 1×10^5 Hz to 1×10^3 Hz, the flat portion illustrates the solution resistance [66], (ii) the inclined phase in the frequency range of 1×10^3 Hz to 1×10^{-1} Hz. The impedance increases up to 1×10^6 Ω cm^2 during this phase. Moreover, the phase angle close to 90° demonstrates a denser passive oxide film [18]. In the present work, the Bode phase angle plot displays a wide plateau above phase angle of 80° from middle to low frequency range which illustrates the formation of denser passive oxide films on the surface of both alloys.

Moreover, the SEM-EDX surface analyses were performed in order to confirm the formation of oxides on the surface of T43 and T45 alloys after corrosion tests. Fig. 9a–b shows the formation of oxides on the surface of T43 and T45 (after 1 h immersion into Hank's solution). The similar kind of oxide formation has been reported for Ti−5Cu alloy after corrosion analysis [67]. The formation of oxides on the surface of T43 and T45 alloys has been further confirmed by means of EDX spectrum analysis which was performed on the oxide particles as well as on the surface other than oxide particles. The EDX spectra of T43 and T45 alloys (Fig. 9c–d) exhibit a peak of oxygen besides the peaks of other elements composing the alloys, i.e., Ti, Nb, Mn and Sn suggesting the formation of surface passive film by a mixture of oxides. Hence, the SEM-EDX surface analyses results are in good agreement with results of electrochemical tests. Based on the points discussed above, T43 and T45 alloys exhibit good corrosion resistance for their use in orthopedic implant applications.

4. Conclusions

The present work evaluates the phase, microstructure and mechanical characterizations including and the strengthening mechanisms of the newly designed Ti-26Nb-xZr-yMn (x = 4, 7, 10 wt% and y = 3, 5 wt%) alloys and based on the superior mechanical properties among the investigated alloys the electrochemical kinetics of the Ti-26Nb-4Zr-3Mn Ti-26Nb-4Zr-5Mn alloys. The key findings from this work are summarized as below.

- The phase and microstructural analyses illustrate a monolithic β phase in all the investigated alloys.
- All the investigated alloys exhibit a pronounced true plastic strain (~160%) and a true maximum strength (~950 MPa) and do not show any fracture in compression testing.
- The addition of Mn positively affects the strength of the Ti-Nb-Zr system alloys. The strengthening in the present work is influenced by combined effect of solid-solution, grain-boundary and dislocation strengthening.
- The Ti-26Nb-4Zr-3Mn and Ti-26Nb-4Zr-5Mn alloys demonstrate an improved electrochemical performance as compared to commercially available biomaterials.
- Among the investigated alloys, Ti-26Nb-4Zr-5Mn displays a superior combination of true maximum strength (951 MPa), large true plasticity (162%), highest true yield strength (654 MPa), dislocation density (2.45×10^{15} m^{-2}) and hardness (242 HV) along with improved strain hardening ability and electrochemical kinetics considering the high strain hardening indices (0.42 and 0.09) and low corrosion current density (0.839 nA/cm^2). Therefore, Ti-26Nb-4Zr-5Mn could be the promising candidate for orthopedic implant applications.

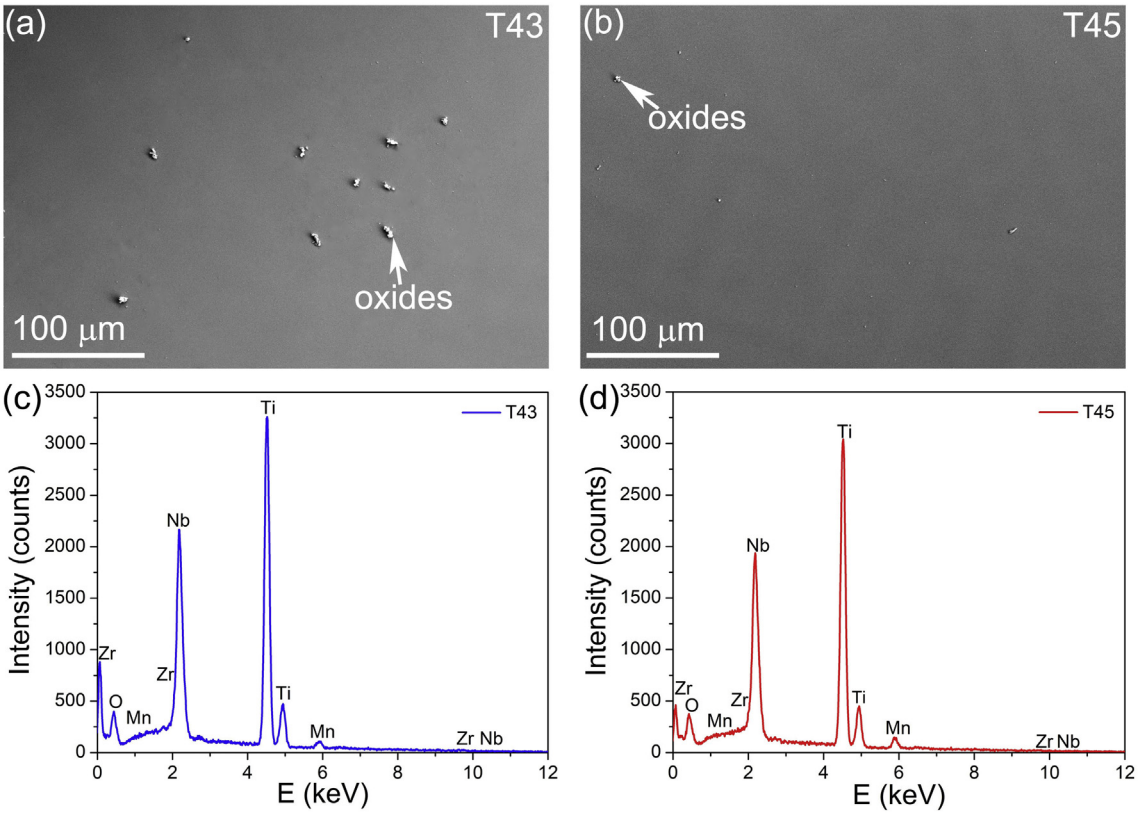

Fig. 9. The SEM micrographs of (a) T43 (b) T45 after corrosion test in Hank's solution and their corresponding EDX spectra (c) T43 (d) T45.

Data availability statement

The raw/processed data required to reproduce these findings cannot be shared at this time as the data also forms part of an ongoing study.

CRediT authorship contribution statement

S.F. Jawed: Conceptualization, Methodology, Investigation, Writing - original draft, Writing - review & editing. **C.D. Rabadia:** Investigation, Writing - review & editing. **Y.J. Liu:** Investigation. **L.Q. Wang:** Investigation. **P. Qin:** Investigation. **Y.H. Li:** Writing - review & editing. **X.H. Zhang:** Writing - review & editing. **L.C. Zhang:** Conceptualization, Methodology, Investigation, Writing - original draft, Writing - review & editing, Supervision.

Declaration of competing interest

There are no known conflicts of interest associated with this publication and there has been no significant financial support for this work that could have influenced its outcome.

Acknowledgements

The authors would like to acknowledge the financial supports provided by open foundation of Guangxi Key Laboratory of Processing for Non-ferrous Metals and Featured Materials, Guangxi University (Grant No. 2019GXYSOF01), National Natural Science Foundation under Grant No. 51674167 and Fundamental Research Funds for the Central Universities in China under Grant No. YG2017ZD06. S.F. Jawed and C.D. Rabadia are grateful for the financial support from the ECU-HEC Joint Scholarship and ECU Postgraduate Research Scholarship, respectively.

References

[1] Y.J. Liu, S.J. Li, L.C. Zhang, Y.L. Hao, T.B. Sercombe, Early plastic deformation behaviour and energy absorption in porous β-type biomedical titanium produced by selective laser melting, Scripta Mater 153 (2018) 99–103, https://doi.org/10.1016/j.scriptamat.2018.05.010.

[2] L.C. Zhang, L.Y. Chen, A review on biomedical titanium alloys: recent progress and prospect, Adv. Eng. Mater. 21 (2019) 1801215, https://doi.org/10.1002/adem.201801215.

[3] Y.J. Liu, Y.S. Zhang, L.C. Zhang, Transformation-induced plasticity and high strength in beta titanium alloy manufactured by selective laser melting, Materialia 6 (2019) 100299, https://doi.org/10.1016/j.mtla.2019.100299.

[4] Y. Abdelrhman, M.A.H. Gepreel, S. Kobayashi, S. Okano, T. Okamoto, Biocompatibility of new low-cost (α + β)-type Ti-Mo-Fe alloys for long-term implantation, Mater. Sci. Eng. C 99 (2019) 552–562, https://doi.org/10.1016/j.msec.2019.01.133.

[5] S. Acharya, S. Bahl, S.S. Dabas, S. Hassan, V. Gopal, A.G. Panicker, G. Manivasagam, S. Suwas, K. Chatterjee, Role of aging induced α precipitation on the mechanical and tribocorrosive performance of a β Ti-Nb-Ta-O orthopedic alloy, Mater. Sci. Eng. C. 103 (2019) 109755, , https://doi.org/10.1016/j.msec.2019.109755.

[6] J.M. Cordeiro, V.A. Barão, Is there scientific evidence favoring the substitution of commercially pure titanium with titanium alloys for the manufacture of dental implants? Mater. Sci. Eng. C 71 (2017) 1201–1215, https://doi.org/10.1016/j.msec.2016.10.025.

[7] Y. Liu, S. Li, W. Hou, S. Wang, Y. Hao, R. Yang, T.B. Sercombe, L.-C. Zhang, Electron beam melted beta-type Ti–24Nb–4Zr–8Sn porous structures with high strength-to-modulus ratio, J. Mater. Sci. Technol. 32 (2016) 505–508, https://doi.org/10.1016/j.jmst.2016.03.020.

[8] S.F. Jawed, C.D. Rabadia, Y.J. Liu, L.Q. Wang, Y.H. Li, X.H. Zhang, L.C. Zhang, Mechanical characterization and deformation behavior of β-stabilized Ti-Nb-Sn-Cr alloys, J. Alloys Compd. 792 (2019) 684–693, https://doi.org/10.1016/j.jallcom.2019.04.079.

[9] C.D. Rabadia, Y.J. Liu, L.Y. Chen, S.F. Jawed, L.Q. Wang, H. Sun, L.C. Zhang, Deformation and strength characteristics of Laves phases in titanium alloys, Mater. Des. 179 (2019) 107891, https://doi.org/10.1016/j.matdes.2019.107891.

[10] L. Wang, L. Xie, Y. Lv, L.-C. Zhang, L. Chen, Q. Meng, J. Qu, D. Zhang, W. Lu, Microstructure evolution and superelastic behavior in Ti-35Nb-2Ta-3Zr alloy processed by friction stir processing, Acta Mater. 131 (2017) 499–510, https://doi.org/10.1016/j.actamat.2017.03.079.

[11] D. Sri Maha Vishnu, J. Sure, Y. Liu, R. Vasant Kumar, C. Schwandt, Electrochemical synthesis of porous Ti-Nb alloys for biomedical applications, Mater. Sci. Eng. C 96 (2019) 466–478, https://doi.org/10.1016/j.msec.2018.11.025.

[12] R. Karre, B.K. Kodli, A. Rajendran, N. J, D.K. Pattanayak, K. Ameyama, S.R. Dey, Comparative study on Ti-Nb binary alloys fabricated through spark plasma sintering and conventional P/M routes for biomedical application, Mater. Sci. Eng. C 94 (2019) 619–627, https://doi.org/10.1016/j.msec.2018.10.006.

[13] M. Dinu, S. Franchi, V. Pruna, C.M. Cotrut, V. Secchi, M. Santi, I. Titorencu, C. Battocchio, G. Iucci, A. Vladescu, 2.4 - Ti-Nb-Zr system and its surface biofunctionalization for biomedical applications, in: F.H. Froes, M. Qian (Eds.), Titanium in Medical and Dental Applications, Woodhead Publishing, 2018, pp. 175–200.

[14] M. Kaur, K. Singh, Review on titanium and titanium based alloys as biomaterials for orthopaedic applications, Mater. Sci. Eng. C 102 (2019) 844–862, https://doi.org/10.1016/j.msec.2019.04.064.

[15] A. Madhan Kumar, A.Y. Adesina, M.A. Hussein, S. Ramakrishna, N. Al-Aqeeli, S. Akhtar, S. Saravanan, PEDOT/FHA nanocomposite coatings on newly developed Ti-Nb-Zr implants: biocompatibility and surface protection against corrosion and bacterial infections, Mater. Sci. Eng. C 98 (2019) 482–495, https://doi.org/10.1016/j.msec.2019.01.012.

[16] H. Hu, L. Zhang, Z. He, Y. Jiang, J. Tan, Microstructure evolution, mechanical properties, and enhanced bioactivity of Ti-13Nb-13Zr based calcium pyrophosphate composites for biomedical applications, Mater. Sci. Eng. C 98 (2019) 279–287, https://doi.org/10.1016/j.msec.2018.12.137.

[17] S. Ozan, J. Lin, Y. Li, Y. Zhang, K. Munir, H. Jiang, C. Wen, Deformation mechanism and mechanical properties of a thermomechanically processed β Ti–28Nb–35.4Zr alloy, J. Mech. Behav. Biomed. Mater. 78 (2018) 224–234, https://doi.org/10.1016/j.jmbbm.2017.11.025.

[18] J.C. Wang, Y.J. Liu, P. Qin, S.X. Liang, T.B. Sercombe, L.C. Zhang, Selective laser melting of Ti–35Nb composite from elemental powder mixture: microstructure, mechanical behavior and corrosion behavior, Mater. Sci. Eng. A 760 (2019) 214–224, https://doi.org/10.1016/j.msea.2019.06.001.

[19] C.D. Rabadia, Y.J. Liu, G.H. Cao, Y.H. Li, C.W. Zhang, T.B. Sercombe, H. Sun, L.C. Zhang, High-strength β stabilized Ti-Nb-Fe-Cr alloys with large plasticity, Mater. Sci. Eng. A 732 (2018) 368–377, https://doi.org/10.1016/j.msea.2018.07.031.

[20] J. Wang, Q. Li, C. Xiong, Y. Li, B. Sun, Effect of Zr on the martensitic transformation and the shape memory effect in Ti-Zr-Nb-Ta high-temperature shape memory alloys, J. Alloys Compd. 737 (2018) 672–677, https://doi.org/10.1016/j.jallcom.2017.12.003.

[21] S.F. Jawed, C.D. Rabadia, Y.J. Liu, L.Q. Wang, Y.H. Li, X.H. Zhang, L.C. Zhang, Beta-type Ti-Nb-Zr-Cr alloys with large plasticity and significant strain hardening, Mater. Des. 181 (2019) 108064, , https://doi.org/10.1016/j.matdes.2019.108064.

[22] N. Kamikawa, K. Sato, G. Miyamoto, M. Murayama, N. Sekido, K. Tsuzaki, T. Furuhara, Stress–strain behavior of ferrite and bainite with nano-precipitation in low carbon steels, Acta Mater. 83 (2015) 383–396, https://doi.org/10.1016/j.actamat.2014.10.010.

[23] X.X. Ye, B. Chen, J.H. Shen, J. Umeda, K. Kondoh, Microstructure and strengthening mechanism of ultrastrong and ductile Ti-xSn alloy processed by powder metallurgy, J. Alloys Compd. 709 (2017) 381–393, https://doi.org/10.1016/j.jallcom.2017.03.171.

[24] X.X. Ye, H. Imai, J.H. Shen, B. Chen, G.Q. Han, J. Umeda, M. Takahashi, K. Kondoh, Strengthening-toughening mechanism study of powder metallurgy Ti-Si alloy by interrupted in-situ tensile tests, J. Alloys Compd. 694 (2017) 82–92, https://doi.org/10.1016/j.jallcom.2016.09.319.

[25] J.Y. He, H. Wang, H.L. Huang, X.D. Xu, M.W. Chen, Y. Wu, X.J. Liu, T.G. Nieh, K. An, Z.P. Lu, A precipitation-hardened high-entropy alloy with outstanding tensile properties, Acta Mater. 102 (2016) 187–196, https://doi.org/10.1016/j.actamat.2015.08.076.

[26] P.F. Santos, M. Niinomi, H. Liu, K. Cho, M. Nakai, A. Trenggono, S. Champagne, H. Hermawan, T. Narushima, Improvement of microstructure, mechanical and corrosion properties of biomedical Ti-Mn alloys by Mo addition, Mater. Des. 110 (2016) 414–424, https://doi.org/10.1016/j.matdes.2016.07.115.

[27] Z. Chen, Y. Liu, H. Jiang, M. Liu, C.H. Wang, G.H. Cao, Microstructures and mechanical properties of Mn modified, Ti-Nb-based alloys, J. Alloys Compd. 723 (2017) 1091–1097, https://doi.org/10.1016/j.jallcom.2017.06.311.

[28] P.F. Santos, M. Niinomi, K. Cho, M. Nakai, H. Liu, N. Ohtsu, M. Hirano, M. Ikeda, T. Narushima, Microstructures, mechanical properties and cytotoxicity of low cost beta Ti–Mn alloys for biomedical applications, Acta Biomater. 26 (2015) 366–376, https://doi.org/10.1016/j.actbio.2015.08.015.

[29] M. Abdel-Hady, K. Hinoshita, M. Morinaga, General approach to phase stability and elastic properties of β-type Ti-alloys using electronic parameters, Scripta Mater 55 (2006) 477–480, https://doi.org/10.1016/j.scriptamat.2006.04.022.

[30] C.D. Rabadia, Y.J. Liu, L. Wang, H. Sun, L.C. Zhang, Laves phase precipitation in Ti-Zr-Fe-Cr alloys with high strength and large plasticity, Mater. Des. 154 (2018) 228–238, https://doi.org/10.1016/j.matdes.2018.05.035.

[31] G.K. Williamson, R.E. Smallman, III. Dislocation densities in some annealed and cold-worked metals from measurements on the X-ray debye-scherrer spectrum, Philos. Mag. 1 (1956) 34–46, https://doi.org/10.1080/14786435608238074.

[32] R. Huang, Y. Han, The effect of SMAT-induced grain refinement and dislocations on the corrosion behavior of Ti–25Nb–3Mo–3Zr–2Sn alloy, Mater. Sci. Eng. C 33 (2013) 2353–2359, https://doi.org/10.1016/j.msec.2013.01.068.

[33] G.K. Williamson, W.H. Hall, X-ray line broadening from filed aluminium and wolfram, Acta Metall. 1 (1953) 22–31, https://doi.org/10.1016/0001-6160(53)90006-6.

[34] K. Bazzi, A. Rathi, V.M. Meka, R. Goswami, T.V. Jayaraman, Significant reduction in intrinsic coercivity of high-entropy alloy FeCoNiAl0.375Si0.375 comprised of supersaturated f.c.c. phase, Materialia 6 (2019) 100293, , https://doi.org/10.1016/j.mtla.2019.100293.

[35] C.D. Rabadia, Y.J. Liu, C.H. Zhao, J.C. Wang, S.F. Jawed, L.Q. Wang, L.Y. Chen, H. Sun, L.C. Zhang, Improved trade-off between strength and plasticity in titanium based metastable beta type Ti-Zr-Fe-Sn alloys, Mater. Sci. Eng. A 766 (2019) 138340, https://doi.org/10.1016/j.msea.2019.138340.

[36] C.D. Rabadia, Y.J. Liu, S.F. Jawed, L. Wang, Y.H. Li, X.H. Zhang, T.B. Sercombe, H. Sun, L.C. Zhang, Improved deformation behavior in Ti-Zr-Fe-Mn alloys comprising the C14 type Laves and β phases, Mater. Des. 160 (2018) 1059–1070, https://doi.org/10.1016/j.matdes.2018.10.049.

[37] H.Y. Kim, J. Fu, H. Tobe, J.I. Kim, S. Miyazaki, Crystal structure, transformation strain, and superelastic property of Ti–Nb–Zr and Ti–Nb–Ta alloys, Shap. Mem. Superelasticity 1 (2015) 107–116, https://doi.org/10.1007/s40830-015-0022-3.

[38] A. Biesiekierski, D. Ping, Y. Li, J. Lin, K.S. Munir, Y. Yamabe-Mitarai, C. Wen, Extraordinary high strength Ti-Zr-Ta alloys through nanoscaled, dual-cubic spinodal reinforcement, Acta Biomater. 53 (2017) 549–558, https://doi.org/10.1016/j.actbio.2017.01.085.

[39] M.J. Bermingham, S.D. McDonald, M.S. Dargusch, D.H. StJohn, Grain-refinement mechanisms in titanium alloys, J. Mater. Res. 23 (2008) 97–104, https://doi.org/10.1557/JMR.2008.0002.

[40] S.J. Dai, Y. Wang, F. Chen, X.Q. Yu, Y.F. Zhang, Influence of Zr content on microstructure and mechanical properties of implant Ti–35Nb–4Sn–6Mo–xZr alloys, T. Nonferr. Metal. Soc. 23 (2013) 1299–1303, https://doi.org/10.1016/S1003-6326(13)62597-2.

[41] C. Lee, W. Ho, C.-P. Ju, J.C. Lin, Structure and properties of titanium–25 niobium–x iron alloys, J. Mater. Sci. Mater. Med. 13 (2002) 695–700, https://doi.org/10.1023/A:1015798011434.

[42] L.-C. Zhang, H.-B. Lu, C. Mickel, J. Eckert, Ductile ultrafine-grained Ti-based alloys with high yield strength, Appl. Phys. Lett. 91 (2007) 051906, , https://doi.org/10.1063/1.2766861.

[43] L.C. Zhang, J. Das, H.B. Lu, C. Duhamel, M. Calin, J. Eckert, High strength Ti–Fe–Sn ultrafine composites with large plasticity, Scripta Mater 57 (2007) 101–104, https://doi.org/10.1016/j.scriptamat.2007.03.031.

[44] M. Bönisch, M. Calin, J. van Humbeeck, W. Skrotzki, J. Eckert, Factors influencing the elastic moduli, reversible strains and hysteresis loops in martensitic Ti–Nb alloys, Mater. Sci. Eng. C 48 (2015) 511–520, https://doi.org/10.1016/j.msec.2014.12.048.

[45] J. Chakrabarty, Applied Plasticity, second ed., Springer-Verlag, USA, 2000, https://doi.org/10.1152/jn.2000.84.5.2582.

[46] S. Ozan, J. Lin, Y. Li, R. Ipek, C. Wen, Development of Ti–Nb–Zr alloys with high elastic admissible strain for temporary orthopedic devices, Acta Biomater. 20 (2015) 176–187, https://doi.org/10.1016/j.actbio.2015.03.023.

[47] A. Shabani, M.R. Toroghinejad, A. Shafyei, P. Cavaliere, Effect of cold-rolling on microstructure, texture and mechanical properties of an equiatomic FeCrCuMnNi high entropy alloy, Materialia 1 (2018) 175–184, https://doi.org/10.1016/j.mtla.2018.06.004.

[48] G.H. Zhao, X.Z. Liang, B. Kim, P.E.J. Rivera-Díaz-del-Castillo, Modelling strengthening mechanisms in beta-type Ti alloys, Mater. Sci. Eng. A 756 (2019) 156–160, https://doi.org/10.1016/j.msea.2019.04.027.

[49] L.A. Gypen, A. Deruyttere, The combination of atomic size and elastic modulus misfit interactions in solid solution hardening, Scripta Metall 15 (1981) 815–820, https://doi.org/10.1016/0036-9748(81)90257-X.

[50] I. Toda-Caraballo, P.E.J. Rivera-Díaz-del-Castillo, Modelling solid solution hardening in high entropy alloys, Acta Mater. 85 (2015) 14–23, https://doi.org/10.1016/j.actamat.2014.11.014.

[51] L.A. Gypen, A. Deruyttere, Multi-component solid solution hardening, J. Mater. Sci. 12 (1977) 1028–1033, https://doi.org/10.1007/bf00540987.

[52] D. Wu, J. Zhang, J.C. Huang, H. Bei, T.G. Nieh, Grain-boundary strengthening in nanocrystalline chromium and the Hall–Petch coefficient of body-centered cubic metals, Scripta Mater 68 (2013) 118–121, https://doi.org/10.1016/j.scriptamat.2012.09.025.

[53] Z.C. Cordero, B.E. Knight, C.A. Schuh, Six decades of the Hall–Petch effect – a survey of grain-size strengthening studies on pure metals, Int. Mater. Rev. 61 (2016) 495–512, https://doi.org/10.1080/09506608.2016.1191808.

[54] Z. Fan, P. Tsakiropoulos, P.A. Smith, A.P. Miodownik, Extension of the Hall-Petch relation to two-ductile-phase alloys, Philos. Mag. A 67 (1993) 515–531, https://doi.org/10.1080/01418619308207175.

[55] R. Madec, B. Devincre, L. Kubin, From dislocation junctions to forest hardening, Phys. Rev. Lett. 89 (2002) 255508, , https://doi.org/10.1103/PhysRevLett.89.255508.

[56] H. Yang, S. Kano, J. Shen, J. McGrady, Z. Zhao, Z. Duan, H. Abe, On the strength-hardness relationships in a Zr-Nb alloy plate with bimodal basal texture microstructure, Mater. Sci. Eng. A 732 (2018) 333–340, https://doi.org/10.1016/j.msea.2018.07.028.

[57] H.-G. Kim, I.-H. Kim, J.-Y. Park, Y.-H. Koo, Influence of alloy composition on work hardening behavior of zirconium-based alloys, Nucl. Eng. Technol. 45 (2013) 505–512, https://doi.org/10.5516/NET.07.2012.055.

[58] P. Li, Microstructure and mechanical properties of novel B2-type ductile Zr–Co–Cu alloys containing the B33 phase, Mater. Res. Express. 4 (2017) 086505, , https://doi.org/10.1088/2053-1591/aa80fc.

[59] C. Zhao, X. Chen, F. Pan, J. Wang, S. Gao, T. Tu, C. Liu, J. Yao, A. Atrens, Strain hardening of as-extruded Mg-xZn (x = 1, 2, 3 and 4 wt%) alloys, J. Mater. Sci. Technol. 35 (2019) 142–150, https://doi.org/10.1016/j.jmst.2018.09.015.

[60] K. Miyakusu, Y. Uematsu, K. Hoshino, Effect of alloying elements on strain hardening exponent of ferritic stainless steel, Trans. Iron Steel Inst. Jpn. 26 (1986) 228–235, https://doi.org/10.2355/isijinternational1966.26.228.

[61] A.I.O. Zaid, S.M.A. Al-Qawabah, Effect of Zr addition on the mechanical characteristics and wear resistance of Al grain refined by Ti after extrusion, IOP

Conference Ser.: Mater. Sci. Eng. 146 (2016) 012023, , https://doi.org/10.1088/1757-899x/146/1/012023.
[62] Z. Fan, H. Mingzhi, S. Deke, The relationship between the strain-hardening exponent n and the microstructure of metals, Mater. Sci. Eng. A 122 (1989) 211–213, https://doi.org/10.1016/0921-5093(89)90632-1.
[63] R. Silva, A. Pinto, A. Kuznetsov, I. Bott, Precipitation and grain size effects on the tensile strain-hardening exponents of an API X80 steel pipe after high-frequency hot-induction bending, Metals 8 (2018) 168, https://doi.org/10.3390/met8030168.
[64] S. Nagarjuna, B. Gopalakrishna, M. Srinivas, On the strain hardening exponent of Cu–26Ni–17Zn alloy, Mater. Sci. Eng. A 429 (2006) 169–172, https://doi.org/10.1016/j.msea.2006.05.096.
[65] J. Zhang, F. Sun, Z. Chen, Y. Yang, B. Shen, J. Li, F. Prima, Strong and ductile beta Ti–18Zr–13Mo alloy with multimodal twinning, Materials Research Letters 7 (2019) 251–257, https://doi.org/10.1080/21663831.2019.1595763.
[66] P. Qin, Y. Chen, Y.-J. Liu, J. Zhang, L.-Y. Chen, Y. Li, X. Zhang, C. Cao, H. Sun, L.-C. Zhang, Resemblance in corrosion behavior of selective laser melted and traditional monolithic β Ti-24Nb-4Zr-8Sn alloy, ACS Biomater. Sci. Eng. 5 (2019) 1141–1149, https://doi.org/10.1021/acsbiomaterials.8b01341.
[67] P. Qin, Y. Liu, T.B. Sercombe, Y. Li, C. Zhang, C. Cao, H. Sun, L.-C. Zhang, Improved corrosion resistance on selective laser melting produced Ti-5Cu alloy after heat treatment, ACS Biomater. Sci. Eng. 4 (2018) 2633–2642, https://doi.org/10.1021/acsbiomaterials.8b00319.